

Atomic-Scale Control of Electronic Structure and Ferromagnetic Insulating State in Perovskite Oxide Superlattices by Long-Range Tuning of BO_6 Octahedra

Weiwei Li,* Bonan Zhu, Ruixue Zhu, Qiang Wang, Ping Lu, Yuanwei Sun, Clodomiro Cafolla, Zhimin Qi, Aiping Chen, Peng Gao, Haiyan Wang, Qing He,* Kelvin H. L. Zhang,* and Judith L. MacManus-Driscoll*

Control of BO_6 octahedral rotations at the heterointerfaces of dissimilar ABO_3 perovskites has emerged as a powerful route for engineering novel physical properties. However, its impact length scale is constrained at 2–6 unit cells close to the interface and the octahedral rotations relax quickly into bulk tilt angles away from interface. Here, a long-range (up to 12 unit cells) suppression of MnO_6 octahedral rotations in $\text{La}_{0.9}\text{Ba}_{0.1}\text{MnO}_3$ through the formation of superlattices with SrTiO_3 can be achieved. The suppressed MnO_6 octahedral rotations strongly modify the magnetic and electronic properties of $\text{La}_{0.9}\text{Ba}_{0.1}\text{MnO}_3$ and hence create a new ferromagnetic insulating state with enhanced Curie temperature of 235 K. The emergent properties in $\text{La}_{0.9}\text{Ba}_{0.1}\text{MnO}_3$ arise from a preferential occupation of the out-of-plane Mn $d_{3z^2-r^2}$ orbital and a reduced Mn e_g bandwidth, induced by the suppressed octahedral rotations. The realization of long-range tuning of BO_6 octahedra via superlattices can be applicable to other strongly correlated perovskites for exploring new emergent quantum phenomena.

1. Introduction


Transition metal perovskite oxides, ABO_3 , exhibit a broad range of physical properties such as metal–insulator transitions, superconductivity and colossal magnetoresistance. These fascinating properties are essentially determined by the interlinked and corner-connected BO_6 octahedra,^[1,2] whose bond lengths and bond angles determine the hybridization between transition metal nd and oxygen $2p$ orbitals, significantly altering the interplay between spin, charge, and orbital and lattice degrees of freedom.^[3,4] Therefore, tuning of the BO_6 octahedra is a key knob for the design of perovskite oxides with novel physical properties. In bulk compounds, the modulation of BO_6

Dr. W.-W. Li, Dr. B. Zhu, Prof. J. L. MacManus-Driscoll
Department of Materials Science and Metallurgy
University of Cambridge
27 Charles Babbage Road, Cambridge CB3 0FS, UK
E-mail: wl337@cam.ac.uk; jld35@cam.ac.uk

R. Zhu, Y. Sun, Prof. P. Gao
International Centre for Quantum Materials
and Electron Microscopy Laboratory
School of Physics
Peking University
Beijing 100871, China

Dr. Q. Wang
Department of Physics and Astronomy
West Virginia University
Morgantown, WA 26506, USA

Dr. P. Lu
Sandia National Laboratories
Albuquerque, NM 87185, USA

 The ORCID identification number(s) for the author(s) of this article can be found under <https://doi.org/10.1002/adfm.202001984>.

© 2020 The Authors. Published by Wiley-VCH GmbH. This is an open access article under the terms of the Creative Commons Attribution License, which permits use, distribution and reproduction in any medium, provided the original work is properly cited.

C. Cafolla, Dr. Q. He
Department of Physics
Durham University
Durham DH1 3LE, UK
E-mail: qing.he@durham.ac.uk

Z. Qi, Prof. H. Wang
School of Materials Engineering
Purdue University
West Lafayette, IN 47907, USA

Dr. A. Chen
Center for Integrated Nanotechnologies
Los Alamos National Laboratory
Los Alamos, NM 87545, USA

Prof. P. Gao
Collaborative Innovation Center for Quantum Matter
Beijing 100871, China

Prof. K. H. L. Zhang
State Key Laboratory of Physical Chemistry of Solid Surfaces
College of Chemistry and Chemical Engineering
Xiamen University
Xiamen 361005, China
E-mail: kelvinzhang@xmu.edu.cn

DOI: 10.1002/adfm.202001984

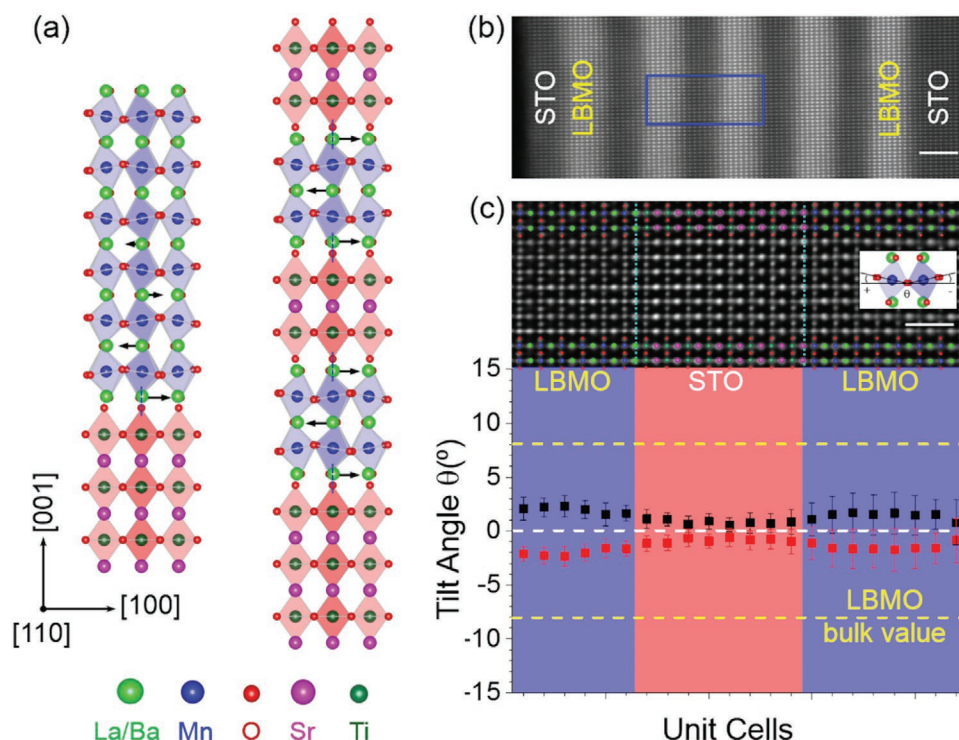


Figure 1. a) Schematic view of octahedral rotation modulation for plain LBMO (blue) on STO (red) substrate (left panel) and for L2S2 superlattice on STO substrate (right panel). The black arrows and their lengths indicate the direction and amount of the rotation angle change, respectively. b) Annular dark field (ADF)-STEM image of L2S2 superlattice, viewed from the pseudo cubic [110] direction. The scale bar is 3 nm. c) Top panel: Integrated differential phase-contrast (iDPC) STEM image, corresponding to blue rectangle region in b. The atom columns are marked by different colors. The scale bar is 1 nm. Bottom panel: Plane-averaged octahedral tilt angles of LBMO and STO.

bond lengths and octahedral rotations are usually realized by substituting isovalent cations with different ionic radius, changing the temperature or applying high pressure.^[5–8] In perovskite oxide heterostructures, the BO_6 octahedra can be tailored by strain engineering (or substrate-induced lattice mismatch strain) and interfacial coupling at the heterointerfaces between dissimilar perovskites, providing a new platform for engineering novel electronic and ferroic ground states that are hard or even impossible to achieve in bulk.^[2,9–19]

Strain engineering has been widely used for tuning the physical properties of perovskite oxide heterostructures. However, atomic-scale control of BO_6 octahedral rotations is difficult to achieve directly by the tuning of epitaxial strain, because strain effects are rather complex and are usually accompanied by other effects such as structural changes, oxygen vacancies, etc.^[2,19,20] On the other hand, recent studies have demonstrated that oxygen octahedral coupling (OOC) at the heterointerfaces can delicately tailor the local BO_6 octahedral rotations at an atomic-scale without disturbing other structural changes, thus creating emergent electronic phases and functionalities.^[15–17] However, as shown in the left sketch in **Figure 1a**, the major drawback of OOC is that its impact length scale is only 2–6 unit cells (uc) confined at the interface region, and the modulation of BO_6 octahedral rotations decays very quickly away from interface.^[15–17,21–24] Therefore, an enhancement of the impact length is highly desirable in order to extend the tuning of emergent effects beyond the interfacial region and to achieve a large volume of material, comprising novel functionalities for both fundamental studies and device applications.

Amongst perovskite oxide-based systems, heterostructures composed of magnetic materials are especially fascinating, such as the ferromagnetism discovered at interfaces between two antiferromagnets or even between a paramagnet and an antiferromagnet.^[25–28] Such magnetic interfaces are also highly important for technological applications such as next-generation dissipationless quantum electronic and spintronic devices. Ferromagnetic insulators with Curie temperatures (T_C) above room temperature and forming coherent interface with electrodes are strongly needed for generating pure spin-polarized currents for spintronic devices.^[29,30] Unfortunately, current promising ferromagnetic insulating materials have a T_C significantly lower than room temperature.^[31] Consequently, ferromagnetic insulators with a higher T_C are highly desirable to be explored.

Bulk $\text{La}_{0.9}\text{Ba}_{0.1}\text{MnO}_3$ (LBMO, pseudocubic lattice parameter ≈ 3.89 Å) is a ferromagnetic insulator with a T_C of ≈ 185 K.^[32] However, when grown as a thin film, LBMO exhibits a ferromagnetic metallic state with T_C of 250–295 K.^[32] The origin of the ferromagnetic metallic state with increased T_C is still not fully understood, but both cationic vacancies and strain offer possible explanations.^[32,33] The physical properties of LBMO, similar to other manganites, is highly susceptible to the MnO_6 octahedral rotations.^[15,17] At room temperature, bulk LBMO exhibits an orthorhombic structure with $a^-a^-c^+$ rotation pattern ($Pbnm$), and with Mn–O–Mn angles of 159.20° (in-plane) and 162.18° (out-of-plane) and Mn–O bond lengths of 1.986 Å (in-plane), 2.003 Å, and 1.968 Å (out-of-plane).^[34,35] On the other hand, nonmagnetic SrTiO_3 (STO, lattice parameter ≈ 3.90 Å)

crystallizes into a cubic structure with an $a^0a^0a^0$ pattern ($Pm-3m$).^[35] There is only an $\approx 0.26\%$ lattice mismatch between LBMO and STO which allows us to minimize the unwanted strain effect and associated structural perturbations in LBMO/STO superlattices. By building the superlattices, we can further exclude the effect of symmetry breaking at the free surfaces of epitaxial films with thickness scaling induced extra contribution to the modification of electronic structure and physical properties.^[36] Hence, superlattices give us an opportunity to understand the link between the BO_6 octahedral rotations and electronic structure, as well as novel ferroic and transport properties, which are currently not yet well understood. The symmetry breaking of the crystal and the structural discontinuity of the oxygen octahedra cage at the interfaces, as shown in the right sketch in Figure 1a, makes the LBMO/STO superlattice a prototypical system to investigate the electronic and magnetic ground state via the modification of the BO_6 octahedra with a large impact length scale.

In this study, by carefully growing a series of (LBMO) N -(STO) N (noted as LNS N ; $N = 4, 5, 6, 8, 9, 10, 12$, and 14) superlattices, we demonstrate that the modulation of MnO_6 octahedral rotations in LBMO could be extended up to 12 uc which is significantly increased in comparison to previously reported OOC length scale of 2–6 uc.^[15–17,21–24] O K-edge X-ray absorption spectroscopy (XAS), X-ray magnetic circular dichroism (XMCD) and linear dichroism (XLD) and density functional theory (DFT) calculations reveal that when interfacial MnO_6 octahedral rotations are strongly suppressed, the Mn e_g bandwidth is reduced and orbital reconstructions occur in the Mn 3d orbitals. This in turn modifies the magnetic and electronic ground states of the manganite and creates an emergent ferromagnetic insulating state in LBMO with an increased T_C of 235 K.

2. Results and Discussion

The LBMO/STO superlattice and plain LBMO films were fabricated by pulsed laser deposition (PLD) monitored by in situ reflection high-energy electron-diffraction (RHEED). Structural characterizations, such as X-ray diffraction (XRD), atomic force microscopy (AFM) and X-ray reflectivity (XRR), show the LNS N superlattice films with atomically flat surface, an interfacial roughness of $\approx 4 \text{ \AA}$, high crystalline quality and coherently strained to the STO substrates (Figure S1, Supporting Information). The corresponding annular dark-field scanning transmission electron microscopy (ADF-STEM) images, as shown in Figure 1b and Figure S2a (Supporting Information), further confirm the high-quality of the film with atomically sharp interfaces and the superlattice with designed periodicity. The slightly wavy interfaces observed in Figure S2a (Supporting Information) may be caused by the presence of atomic terraces in the film along the viewing direction. Chemical sharpness was ascertained using atomically resolved energy-dispersive X-ray spectroscopic (EDS) mapping across the LBMO/STO interfaces (Figure S2b, Supporting Information). By considering geometrical roughness and projection effect,^[37–39] the interfacial intermixing was determined to be around 1 uc.

We used integrated differential phase-contrast (iDPC) STEM imaging to directly visualize metal cations and oxygen anions in

the superlattice, from which the displacements of oxygen anions with respect to the cations, i.e., octahedral tilt angles, were quantitatively determined.^[40–43] Figure 1c (top panel) shows a representative iDPC image of the LBMO/STO/LBMO layers, viewed from the pseudo cubic [110] direction. Using iDPC image, the TiO_6 rotation pattern in the STO layer is confirmed as $a^0a^0a^0$, consistent with the $Pm-3m$ space group of bulk STO.^[35] The plane averaged and projected tilt angles across LBMO/STO interfaces were further determined from the iDPC image, shown in the bottom panel of Figure 1c. It can be seen that the tilt angles in the LBMO layers are around 1° – 2° , which are much smaller than the bulk value of 8° , indicating that the MnO_6 octahedral rotations are significantly suppressed by the OOC in the superlattice. In sharp contrast to a short impact length of OOC ($\approx 3 \text{ uc}$) and a much smaller suppression of MnO_6 rotation angles (from 4.5° to 8°) in a plain LBMO film directly grown on an STO substrate (Figure S3, Supporting Information), the impact length scale of OOC within the LBMO layers in the superlattice is considerably increased to be over 8 uc and the suppression of MnO_6 octahedral rotations is very obvious. In addition, we also observed that there is a small difference in tilt angles between the interfacial ($\approx 1^\circ$) and the interior ($\approx 2^\circ$) LBMO layers.

Soft XAS at the manganese L-edges and oxygen K-edge were performed to investigate the effect of OOC on the electronic structure. Assuming a fully ionic charge assignment using the nominal valence for each layer, the LBMO/STO interfaces have a polar discontinuity at the interface with charge density of $-0.9q(\text{MnO}_2)/+0.9q(\text{La}_{0.9}\text{Ba}_{0.1}\text{O})/0q(\text{TiO}_2)/0q(\text{SrO})$. We found that, compared to the plain LBMO films, there is a change of peak position of the Mn L_3 -edge in the L8S8 superlattice (Figure S4, Supporting Information), which could be caused by the electronic reconstruction within a polar catastrophe scenario akin to that in $\text{LaMnO}_3/\text{SrTiO}_3$ heterointerfaces.^[44,45] The overall line-shapes of oxygen K-edge for 8 and 40 uc LBMO agrees with the reported spectra of $\text{La}_{0.8}\text{Sr}_{0.2}\text{MnO}_3$,^[46,47] apart from an additional feature at $\approx 531 \text{ eV}$ for 8 uc that arises from Ti 3d–O 2p hybridized states from the STO substrate.^[48] The oxygen K-edge XAS spectrum of the L8S8 superlattice (Figure 2a) shows a substantial reduction in the spectral feature, in comparison with plain LBMO films. The reduction of oxygen K-edge XAS intensity may be induced by a decreased Mn 3d–O 2p hybridization and the signal attenuation from the top STO layer. As indicated by XRD results in Figure S1 (Supporting Information), the L8S8 superlattice film is fully strained to the STO substrate, i.e., the in-plane lattice constant (a) of the film is fixed due to substrate-induced tensile strain. However, in comparison with bulk LBMO (pseudocubic lattice constant $\approx 3.89 \text{ \AA}$) and plain 40 uc LBMO film (out-of-plane lattice constant $\approx 3.88 \text{ \AA}$), we found that the out-of-plane lattice constant (c) is increased to $\approx 3.93 \text{ \AA}$ in the L8S8 superlattice. This indicates that the strongly suppressed MnO_6 octahedral rotations increase both the Mn–O bond lengths ($c/a > 1$) and the Mn–O–Mn bond angles (Figure 1c), which may be mainly responsible for the reduction of Mn 3d–O 2p hybridization observed in the L8S8 superlattice. Compared with plain LBMO films, the pre-edge position of the L8S8 superlattice shifts toward higher photon energy (Figure S5, Supporting Information), suggesting a reduction of Mn e_g bandwidth. In bulk manganites, the Mn e_g bandwidth increases as the decrease of Mn–O bond lengths and the increase of

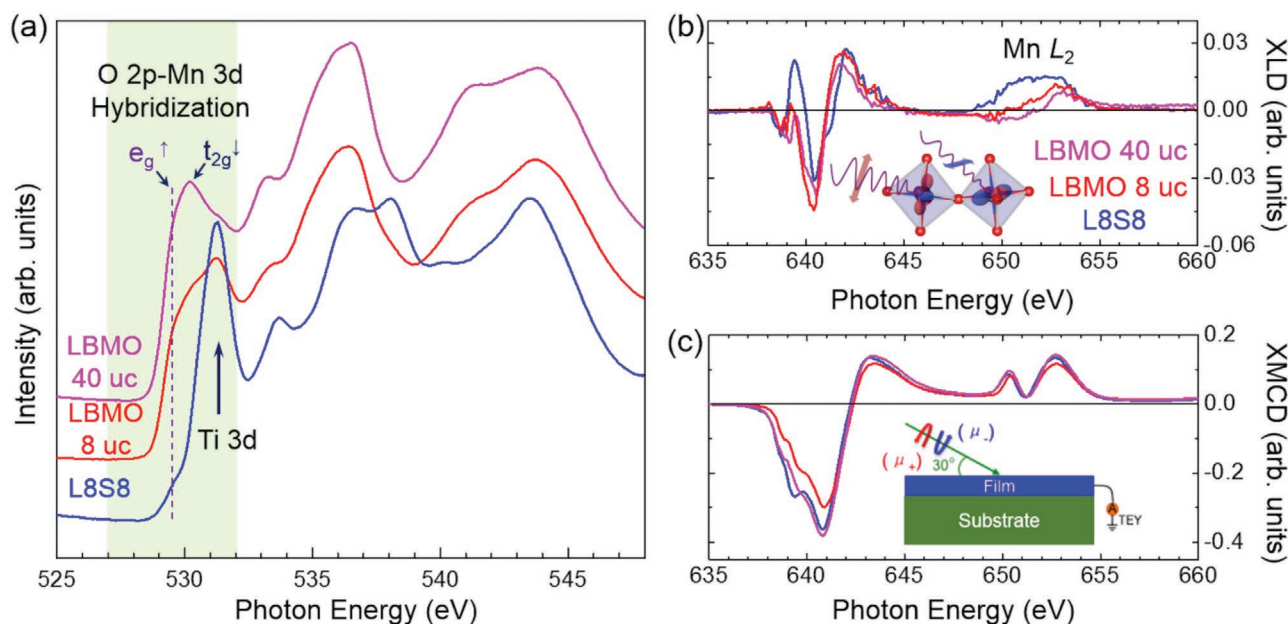


Figure 2. a) XAS O K-edge spectra of plain LBMO and L8S8 superlattice films measured at 300 K. b) XLD and c) XMCD spectra of plain LBMO and L8S8 superlattice films. XMCDs were measured at 4 T and 20 K and XLDs were measured at 300 K without a magnetic field.

Mn–O–Mn bond angles. Using geometry arguments, the suppression of MnO_6 octahedral rotations should increase the lattice constants.^[34,35] However, the in-plane lattice constant of LBMO in the L8S8 superlattice is pinned to that of the STO substrate (3.905 Å), which is smaller than twice that of the Mn–O bond length (1.986 Å) in bulk LBMO.^[34] In this case, for an idealized model where the MnO_6 octahedral rotations are strongly suppressed, this gives rise to a compressive in-plane stress, which increases the out-of-plane Mn–O bond length. This could explain the reduction of Mn e_g bandwidth in the L8S8 superlattice, even though the increase of the Mn–O–Mn bond angles may tend to increase the e_g bandwidth. Similar reduction of bandwidth was reported in the SrIrO_3 films grown on STO substrates when IrO_6 octahedral rotations are strongly suppressed.^[49] We then further investigated the orbital occupancy and magnetic ground states using XLD and XMCD, which provide direct information on the empty Mn 3d orbital states and element-specific information on magnetism, respectively.^[50,51] For the XLD spectra, the smaller (larger) absorption of in-plane polarization suggests more out-of-plane (in-plane) empty states in the e_g band and thus a higher occupancy in the in-plane (out-of-plane) orbitals.^[50] As shown in Figure 2b, the XLD spectrum of L8S8 superlattice shows a pronounced positive signal at the Mn L_2 absorption region (646–657 eV), as compared with the plain LBMO films. The strongly suppressed MnO_6 octahedral rotations cause the elongation along the out-of-plane ($c/a > 1$) in the L8S8 superlattice, leading to a preferential occupation of the out-of-plane $d_{3z^2-r^2}$ orbitals in Mn 3d orbital (Figure S6, Supporting Information).^[50] The unexpected out-of-plane $d_{3z^2-r^2}$ occupancy in the e_g orbital observed in the plain LBMO films under small tensile strain could be caused by the free surface effect.^[50] The line-shapes of the XMCD spectra (Figure 2c) are similar to the reported data of $\text{La}_{0.7}\text{Sr}_{0.3}\text{MnO}_3$.^[52] The XMCD spectra clearly reveal strong dichroism, providing a

solid evidence for a net ferromagnetic moment associated with Mn cations in the films.

Owing to the suppression of MnO_6 octahedral rotations and associated orbital reconstruction within the LBMO layers in the superlattices, we also observed a pronounced change of macroscopic magnetic and transport properties. Magnetic and transport measurements (Figure 3; Figures S7 and S8, Supporting Information) show that the LNSN with $N \leq 12$ exhibit a ferromagnetic insulating state, while the L14S14 superlattice retains a ferromagnetic metallic state similar to plain LBMO films grown on STO substrate. The ferromagnetic insulating T_C of the L12S12 superlattice is around 235 K, which is significantly higher than that of bulk LBMO (185 K).^[32] We attribute this enhanced T_C to the extended modulation of MnO_6 octahedral rotations within LBMO layers in the superlattice. A comparison with plain LBMO films provides further solid evidences of the associated modulation of transport properties by an atomic-scale control of MnO_6 octahedral rotations. As shown in Figure 3b, plain LBMO films (8 and 10 uc) directly grown on STO substrate show a metallic state whereas the L8S8 and L10S10 superlattices show an insulating behavior. We attribute the distinct transport properties of L8S8 and L10S10 superlattices to the reduction of Mn e_g bandwidth via the suppressed MnO_6 octahedral rotations, as revealed by the iDPC image (Figure 1c) and oxygen K-edge XAS (Figure 2a; Figure S5, Supporting Information) studies. Furthermore, the comparison of transport properties between plain LBMO films and LNSN superlattices suggests that the length for the suppression of the MnO_6 octahedral rotations in the superlattices could be up to 12 uc.

To gain further insights into the correlation between the MnO_6 octahedral rotations and its link to the electronic and magnetic structures, we performed first-principles DFT calculations for the L4S4 superlattice. The depth dependence of octahedral rotations across the interfaces (Figure S9a, Supporting

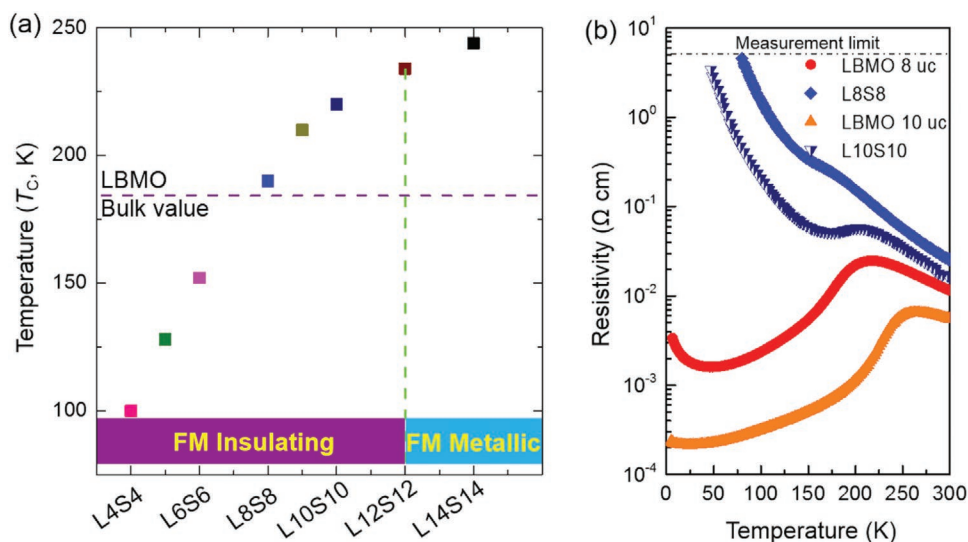


Figure 3. a) Ferromagnetic insulating state to ferromagnetic metallic state transition observed in LNSN superlattices. b) Comparison of resistivity of plain LBMO (8 and 10 uc) films and LNSN ($N = 8$ and 10 uc) superlattices.

Information) shows that the MnO_6 octahedral rotations are suppressed at interfaces, consistent with the suppression of MnO_6 octahedral rotations observed by iDPC images (Figure 1c). Due to the reduction of tilt angle at the LBMO/STO interfaces, we found that the Mn e_g bandwidth of LBMO is reduced from 3.71 eV in the interior layer to 3.22 eV (or 3.34 eV) at the interfacial layers (Figure S9b, Supporting Information) and the hybridization of Mn e_g band–O 2p is reduced through a partial density of states analysis, in agreement with the observation in oxygen K-edge XAS (Figure 2a; Figure S5, Supporting Information) studies. Furthermore, the increased $d_{3z^2-r^2}$ orbital occupancy of e_g band is also supported by the DFT calculations, agreeing well with the XLD results (Figure 2b).

Interestingly, the suppressed MnO_6 octahedral rotations are also accompanied by a change in the local magnetization within the LBMO layers in the superlattices. Polarized neutron reflectometry (PNR) measurements were used to determine quantitatively the depth profile of the magnetization across the L8S8 superlattice. The film was field cooled to the measurement temperature of 25 K with a 1 T field. Figure 4a shows the PNR data with the reflectivity normalized to the asymptotic value of the Fresnel reflectivity, $R_F (= 16\pi^2/Q^4)$. The + (–) sign denotes neutron beam polarization parallel (opposite) to the applied field and corresponds to reflectivities, $R^\pm(Q)$. Q was calculated by $Q = 4\pi \sin(\alpha_i)/\lambda$, where α_i is the angle between the incident neutron beam and the projections on the surface and λ is neutron wavelength. The spin asymmetry [$SA = (R^+ - R^-)/(R^+ + R^-)$], a measure of net magnetization, is shown in Figure 4b. Due to the fact that the nuclear scattering density of LBMO ($3.55e-6/\text{Å}^2$) and STO ($3.53e-6/\text{Å}^2$) are nearly identical, to obtain an unambiguous fitting results of both chemical structure and magnetic structure, the PNR data were fitted together with the XRR data (Figure S1, Supporting Information). For the fitting, the layer thickness and the interface roughness were mainly determined by XRR. We allowed the magnetization of the LBMO layers to vary to achieve the best fit to PNR data.^[53] These set of constraints produced excellent fits

to the reflectivity (Figure 4a) and spin asymmetry (Figure 4b). The obtained magnetic depth profile (Figure 4c) suggests that the interfacial LBMO layers exhibit enhanced magnetization

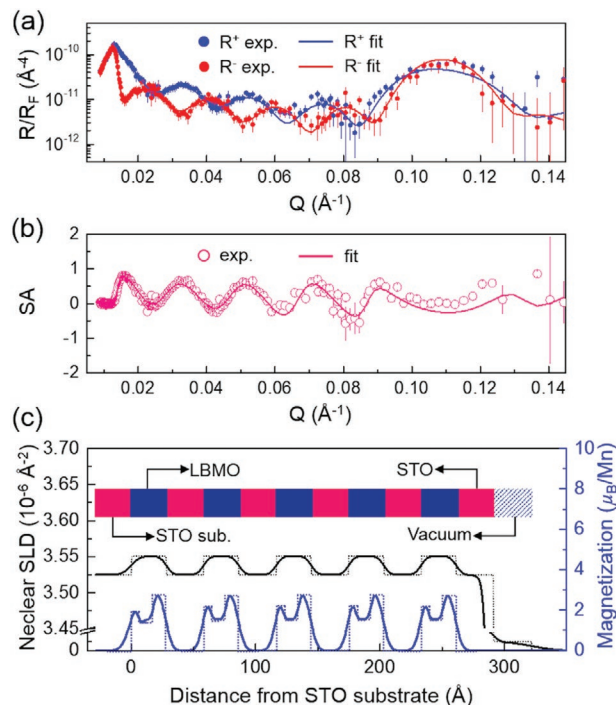


Figure 4. a) Normalized neutron reflectivities (R/R_F) and b) spin asymmetry [$SA = (R^+ - R^-)/(R^+ + R^-)$] of the L8S8 superlattice. $R_F [= (16\pi^2)/Q^4]$ is the Fresnel reflectivity. Symbols represent the experimental results from the neutron measurements. Solid lines are the fits to the experimental data. c) Nuclear scattering length density (nSLD, black line) and magnetic scattering length density (mSLD, blue line) depth profiles obtained from fitting the combined X-ray and neutron reflectivity data. Inset: Schematic drawing of the superlattice geometry. The dashed line represents the mSLD depth profiles with the absolute sharp interfaces.

compared to the interior LBMO layers, as would be expected for the superlattice, where the octahedral rotations very close to the interface are strongly suppressed ($\approx 1^\circ$), while the tilt angle away from the interface increases to $\approx 2^\circ$, as revealed by the iDPC image (Figure 1c). The finding of enhanced magnetization in the interfacial LBMO layers is consistent with previous experimental observation of enhanced magnetization in interfacial $\text{La}_{0.5}\text{Sr}_{0.5}\text{MnO}_3$ and $\text{La}_{0.67}\text{Sr}_{0.33}\text{MnO}_3$ layers via the locally suppressed MnO_6 octahedral rotations.^[23,54] The mechanism of such enhancement in magnetization could be attributed to the subtle competition among the orbital reconstruction, the reduction of Mn e_g bandwidth and the increase of both the Mn–O bond lengths and the Mn–O–Mn bond angles, although the exact nature is still not clear.^[54] The fitting result also suggests an asymmetric magnetization within the LBMO layers close to the interfaces. This can be caused by the asymmetric boundary conditions, such as the interfacial termination, roughness, charge, etc. Similar asymmetric magnetization profiles in the $\text{La}_{0.7}\text{Sr}_{0.3}\text{MnO}_3$ thin films has been observed previously.^[55]

3. Conclusion

In summary, we have employed the LBMO/STO superlattices as a model system to demonstrate an extensive control of MnO_6 octahedral rotations with greatly enhanced OOC impact length of up to 12 uc, compared to the previously reported 2–6 uc.^[15–17,21–24] Suppression of MnO_6 octahedral rotations leads to a change of magnetic exchange interactions, a reduced Mn e_g bandwidth and orbital reconstruction. Consequently, an emergent ferromagnetic insulating state is realized in LBMO with an enhanced T_C of 235 K, which is significantly higher than that of bulk LBMO (185 K). In addition, an enhancement of magnetization in the interfacial LBMO layers is observed with strong coupling to the finely tuned MnO_6 octahedral rotations. Our results also lend themselves to the use of the interface octahedral rotation control in other perovskite materials, opening up new perspectives for the rational design of new classes of quantum materials for next-generation electronic devices.

4. Experimental Section

Film Fabrication and Characterization: (LBMO) N -(STO) N ($N = 4, 5, 6, 8, 9, 10, 12,$ and 14) superlattices with total layer thicknesses of 72–80 uc and plain $\text{La}_{0.9}\text{Ba}_{0.1}\text{MnO}_3$ films were grown on TiO_2 -terminated STO (001) substrates. Both LBMO and STO sublayers were deposited at 750 °C and 100 mTorr oxygen partial pressure from respective stoichiometric targets using the KrF excimer laser (248 nm) with a laser fluence of 1.5 J cm^{-2} . During the growth, in situ reflection high-energy electron-diffraction (RHEED) intensity oscillations were monitored to control the growth at the unit-cell level. After growth, the films were cooled down to room temperature under an oxygen pressure of 300 Torr. Film structures and surface morphologies were investigated by X-ray diffraction (XRD) on a high-resolution X-ray diffractometer (Empyrean, PANalytical, The Netherlands) using Cu $K\alpha$ radiation ($\lambda = 1.5405 \text{ \AA}$) and atomic force microscopy (AFM), respectively.

Scanning Transmission Electron Microscopy: For the L8S8 superlattice, cross-sectional samples oriented along $[110]_{\text{pc}}$ direction for the ADF-STEM and iDPC image acquisition were prepared by slicing, gluing,

grinding, and argon ion milling. The final milling was accomplished by PIPS (Model 691, Gatan Inc.). ADF and iDPC images were recorded at 300 kV using an aberration-corrected FEI Titan Themis G2 with spatial resolutions up to 60 pm. The convergence semiangle for imaging was 30 mrad, the collection semiangles snap was 4–21 mrad for the iDPC imaging, and 39–200 mrad for the ADF. The atom positions were determined by simultaneously fitting with 2D Gaussian peaks using a MATLAB code. The tilt angles are calculated based on the obtained atom positions. A systematic error bar was estimated from the rotation angle observed in the STO substrate. For a plain 26 uc LBMO film, as shown in Figure S3 (Supporting Information), high-angle annular dark-field (HAADF) and annular bright-field (ABF) STEM images were taken using a Nion UltraSTEM operating at 200 kV, equipped with a cold field-emission electron gun and a corrector of third- and fifth-order aberrations. The convergence semiangle for the electron probe was about 30 mrad. HAADF signals for the samples were collected from a detector angle range with an inner collection angle of ≈ 63 mrad. Thirty quickly scanned images ($0.5 \mu\text{s}$ per pixel, with a pixel size of 5–10 pm) were aligned via autocorrelation and displayed as sum image, which was Wiener filtered to reduce noise. Image analysis was done via Digital micrograph and ImageJ scripts.

Magnetic and Transport Characterization: Macroscopic magnetic measurements were performed with a Quantum Design MPMS3 SQUID-VSM magnetometer. Transport measurements were measured by a Quantum Design Physical Property Measurement System (PPMS).

X-Ray Absorption Spectroscopy: X-ray absorption spectroscopy (XAS), X-ray linear dichroism (XLD), and X-ray magnetic circular dichroism (XMCD) measurements at the Mn L-edge were carried out at beamline 4.0.2 at the Advanced Light Source, Lawrence Berkeley National Laboratory. The measurements were performed using the total electron yield (TEY) model and the angle of incident beam was 30° to the sample surface. XMCD measurements were performed at 20 K in a 4 T magnetic field applied in the a – b plane of the films, parallel to the beam propagation direction. To ensure that the XMCD signal was of a magnetic origin, the magnetic field was applied in the opposite direction to verify the sign of the XMCD reversed. XLD measurements were carried out at 300 K without a magnetic field. XLD spectra were obtained by the intensity difference ($I_v - I_h$) between the spectra measured with horizontal (E_h) and vertical (E_v) linear polarizations. The XAS characterization at oxygen K-edge was carried out at the I06 beamline of the Diamond Light Source. The spectra were also collected using a TEY model and the angle of incident beam is 30° to the sample surface.

Polarized Neutron Reflectometry: Polarized neutron reflectometry (PNR) measurements were carried out at BL-4A at the Spallation Neutron Source (SNS), Oak Ridge National Laboratory. A saturating magnetic field of 1 T was applied along the in-plane direction during field cooling and throughout the PNR measurements at 25 K. PNR and XRR data were simulated and fitted by using GenX.^[56] The nuclear scattering length densities (nSLDs) for the LBMO and STO thin films were fixed to their calculated bulk values. The chemical thicknesses of each layer were constrained to the parameters obtained from XRR fitting.

Density Functional Theory Calculations: Density functional theory (DFT) calculations were performed using the plane wave pseudopotential code CASTEP.^[57] A plane wave cut off energy of 700 eV with on-the-fly generated core-corrected ultrasoft pseudopotentials was used. The valence states include 2s and 2p of O, 3s, 3p, 3d, and 4s of Ti, 3s, 3p, 3d, and 4s of Mn, 4s, 4p, and 5s of Sr, 5s, 5p, and 6p of Ba. The Perdew–Burke–Ernzerhof (PBE) exchange–correlation functional was used.^[58] Projected density of states was calculated using OptaDOS^[59] with adaptive broadening.^[60] The simulation cell was consisted of $2 \times 2 \times 4$ unit cells of STO and $2 \times 2 \times 4$ pseudocubic cells of LBMO, as shown in Figure S8 (Supporting Information). The k -points were sampled using a $3 \times 3 \times 1$ Monkhorst–Pack grid. The A-site doping was explicitly introduced by replacing one in eight La atoms with Ba. The Hubbard U correction with $U = 3 \text{ eV}$ was used for the Mn 3d electrons to account for the self-interaction error due to localized electrons.^[61] The lattice constants of the simulation cell

were fixed during the geometry optimization of ionic coordinates. An in-plane pseudocubic lattice constant of 3.98 Å was used to reproduce the experimentally observed biaxial tensile strain in LBMO. Note that the Hubbard *U* correction further increased the equilibrium cell volume of LBMO on top of the PBE level. The cell length in the out-of-plane direction was set to the corresponding multiples of that of the relaxed bulk structures. The STO units were fully constrained to simulate the strong octahedra pinning observed experimentally. The AiiDA framework was used to manage the calculations and preserve their provenance.^[62]

Supporting Information

Supporting Information is available from the Wiley Online Library or from the author.

Acknowledgements

W.-W.L., B.Z., and R. Z. contributed equally to this work. W.-W.L. and J.L.M.-D. acknowledge support from EPSRC Grant EP/L011700/1, EP/N004272/1, and the Isaac Newton Trust (Minute 13.38(k)). J.L.M.-D. acknowledges support from the Royal Academy of Engineering (Grant No. CiET1819_24). B.Z. acknowledges support from China Scholarship Council and Cambridge Commonwealth, European and International Trust. K.H.L.Z. is grateful for funding support from the National Natural Science Foundation of China (Grant No. 21872116). P.G. acknowledges the support from the National Natural Science Foundation of China (Grant Nos. 51672007 and 11974023), the National Key R&D Program of China (Grant No. 2016YFA0300804), Key Area R&D Program of Guangdong Province (2018B010109009), The Key R&D Program of Guangdong Province (2018B030327001), the National Equipment Program of China (ZDYZ2015-1), the “2011 Program” Peking-Tsinghua-IOP Collaborative Innovation Center for Quantum Matter, and Electron Microscopy Laboratory in Peking University for the use of Cs corrected electron microscope. Sandia National Laboratories is a multiprogram laboratory managed and operated by National Technology and Engineering Solutions of Sandia, LLC, a wholly owned subsidiary of Honeywell International, Inc., for the U.S. Department of Energy's National Nuclear Security Administration (NNSA) under contract DE-NA0003525. The work at Los Alamos National Laboratory was supported by the NNSA's Laboratory Directed Research and Development Program and was performed, in part, at the Center for Integrated Nanotechnologies, an Office of Science User Facility operated for the U.S. Department of Energy Office of Science. Los Alamos National Laboratory, an affirmative action equal opportunity employer, is managed by Triad National Security, LLC, for the U.S. Department of Energy's NNSA under contract 89233218CNA000001. Z.Q. and H.W. acknowledge the support from U.S. Naval Research (N00014-16-1-2465) and the U.S. National Science Foundation (DMR-1565822).

Conflict of Interest

The authors declare no conflict of interest.

Keywords

ABO₃ perovskite oxides, BO₆ octahedra, ferromagnetic insulators, interfaces, manganite thin films

Received: March 2, 2020

Revised: June 16, 2020

Published online: August 2, 2020

- [1] M. B. Salamon, M. Jaime, *Rev. Mod. Phys.* **2001**, *73*, 583.
- [2] J. M. Rondinelli, N. A. Spaldin, *Adv. Mater.* **2011**, *23*, 3363.
- [3] Y. Tokura, N. Nagaosa, *Science* **2000**, *288*, 462.
- [4] E. Dagotto, *Science* **2005**, *309*, 257.
- [5] J. B. Torrance, P. Lacorre, A. I. Nazzari, E. J. Ansaldo, C. Niedermayer, *Phys. Rev. B* **1992**, *45*, 8209.
- [6] J. L. Garcia-Munoz, J. Fontcuberta, M. Suaaidi, X. Obradors, *J. Phys.: Condens. Matter* **1996**, *8*, L787.
- [7] J. M. D. Coey, M. Viret, S. V. Molnar, *Adv. Phys.* **1999**, *48*, 167.
- [8] Y. Ding, D. Haskel, Y.-C. Tseng, E. Kaneshita, M. van Veenendaal, J. F. Mitchell, *Phys. Rev. Lett.* **2009**, *102*, 237201.
- [9] H. Y. Hwang, Y. Iwasa, M. Kawasaki, B. Keimer, N. Nagaosa, Y. Tokura, *Nat. Mater.* **2012**, *11*, 103.
- [10] J. Mannhart, D. G. Schlom, *Science* **2010**, *327*, 1607.
- [11] N. Reyren, S. Thiel, A. D. Caviglia, L. Fitting Kourkoutis, G. Hammerl, C. Richter, C. W. Schneider, T. Kopp, A.-S. Rüetschi, D. Jaccard, M. Gabay, D. A. Müller, J.-M. Triscone, J. Mannhart, *Science* **2007**, *317*, 1196.
- [12] J. Chakhalian, J. W. Freeland, H.-U. Habermeier, G. Cristiani, G. Khaliullin, M. van Veenendaal, B. Keimer, *Science* **2007**, *318*, 1114.
- [13] A. Gozar, G. Logvenov, L. Fitting Kourkoutis, A. T. Bollinger, L. A. Giannuzzi, D. A. Müller, I. Bozovic, *Nature* **2008**, *455*, 782.
- [14] J. M. Rondinelli, S. J. May, J. W. Freeland, *MRS Bull.* **2012**, *37*, 261.
- [15] E. J. Moon, R. Colby, Q. Wang, E. Karapetrova, C. M. Schlepütz, M. R. Fitzsimmons, S. J. May, *Nat. Commun.* **2014**, *5*, 5710.
- [16] D. Kan, R. Aso, R. Sato, M. Haruta, H. Kurata, Y. Shimakawa, *Nat. Mater.* **2016**, *15*, 432.
- [17] Z. Liao, M. Huijben, Z. Zhong, N. Gauquelin, S. Macke, R. J. Green, S. Van Aert, J. Verbeeck, G. Van Tendeloo, K. Held, G. A. Sawatzky, G. Koster, G. Rijnders, *Nat. Mater.* **2016**, *15*, 425.
- [18] J. M. Rondinelli, C. J. Fennie, *Adv. Mater.* **2012**, *24*, 1961.
- [19] J. M. Rondinelli, S. Coh, *Phys. Rev. Lett.* **2011**, *106*, 235502.
- [20] A. Vailionis, H. Boschker, W. Siemons, E. P. Houwman, D. H. A. Blank, G. Rijnders, G. Koster, *Phys. Rev. B* **2011**, *83*, 064101.
- [21] Y. Yuan, Y. Lu, G. Stone, K. Wang, C. M. Brooks, D. G. Schlom, S. B. Sinnott, H. Zhou, V. Gopalan, *Nat. Commun.* **2018**, *9*, 5220.
- [22] R. Aso, D. Kan, Y. Shimakawa, H. Kurata, *Cryst. Growth Des.* **2014**, *14*, 2128.
- [23] E. J. Moon, Q. He, S. Ghosh, B. J. Kirby, S. T. Pantelides, A. Y. Borisevich, S. J. May, *Phys. Rev. Lett.* **2017**, *119*, 197204.
- [24] Z. Liao, N. Gauquelin, R. J. Green, K. Müller-Caspary, I. Loboto, L. Li, S. V. Aert, J. Verbeeck, M. Huijben, M. N. Grisolia, V. Rouco, R. E. Hage, J. E. Villegas, A. Mercy, M. Bibes, P. Chosez, G. A. Sawatzky, G. Rijnders, G. Koster, *Proc. Natl. Acad. Sci. USA* **2018**, *115*, 9515.
- [25] K. Ueda, H. Tabata, T. Kawai, *Science* **1998**, *280*, 1064.
- [26] K. S. Takahashi, M. Kawasaki, Y. Tokura, *Appl. Phys. Lett.* **2001**, *79*, 1324.
- [27] C. He, A. J. Grutter, M. Gu, N. D. Browning, Y. Takamura, B. J. Kirby, J. A. Borchers, J. W. Kim, M. R. Fitzsimmons, X. Zhai, V. V. Metha, F. J. Wong, Y. Suzuki, *Phys. Rev. Lett.* **2012**, *109*, 197202.
- [28] A. J. Grutter, H. Yang, B. J. Kirby, M. R. Fitzsimmons, J. A. Aguiar, N. D. Browning, C. A. Jenkins, E. Arenholz, V. V. Mehta, U. S. Alaan, Y. Suzuki, *Phys. Rev. Lett.* **2013**, *111*, 087202.
- [29] T. S. Santos, J. S. Moodera, *Phys. Rev. B* **2004**, *69*, 241203(R).
- [30] M. Gajek, M. Bibes, S. Fusil, K. Bouzehouane, J. Fontcuberta, A. Bathélemy, A. Fert, *Nat. Mater.* **2007**, *6*, 296.
- [31] J. S. Moodera, T. S. Santos, T. Nagahama, *J. Phys.: Condens. Matter* **2007**, *19*, 165202.
- [32] J. Zhang, H. Tanaka, T. Kanki, J.-H. Choi, T. Kawai, *Phys. Rev. B* **2001**, *64*, 184404.
- [33] P. Murugavel, J. H. Lee, J.-G. Yoon, T. W. Noh, J.-S. Chung, M. Heu, S. Yoon, *Appl. Phys. Lett.* **2003**, *82*, 1908.

- [34] B. Dabrowski, K. Rogacki, X. Xiong, P. W. Klamut, R. Dybziński, J. Shaffer, *Phys. Rev. B* **1998**, *58*, 2716.
- [35] A. M. Glazer, *Acta Crystallogr., Sect. B: Struct. Crystallogr. Cryst. Chem.* **1972**, *28*, 3384.
- [36] F. Hellman, A. Hoffmann, Y. Tserkovnyak, G. S. Beach, E. E. Fullerton, C. Leighton, A. H. MacDonald, D. C. Ralph, D. A. Arena, H. A. Dürr, P. Fischer, *Rev. Mod. Phys.* **2017**, *89*, 025006.
- [37] P. Lu, J. Xiong, M. Benthem, Q. Jia, *Appl. Phys. Lett.* **2013**, *102*, 173111.
- [38] S. R. Spurgeon, Y. Du, S. Chambers, *Microsc. Microanal.* **2017**, *23*, 513.
- [39] P. Lu, J. M. Moya, R. Yuan, J. M. Zuo, *Ultramicroscopy* **2018**, *186*, 23.
- [40] I. Lazić, E. G. T. Bosch, S. Lazar, *Ultramicroscopy* **2016**, *160*, 265.
- [41] H. Brown, R. Ishikawa, N. Shibata, Y. Ikuhara, L. J. Allen, S. D. Findlay, *Ultramicroscopy* **2019**, *197*, 112.
- [42] L. Jones, H. Yang, T. J. Pennycook, M. Marshall, S. V. Aert, N. D. Browning, M. R. Castell, P. D. Nellist, *Adv. Struct. Chem. Imaging* **2015**, *1*, 8.
- [43] N. Gauquelin, K. H. W. van den Bos, A. Beche, F. F. Krause, I. Lobato, S. Lazar, A. Rosenauer, S. Van Aert, J. Verbeeck, *Ultramicroscopy* **2017**, *181*, 178.
- [44] Z. H. Chen, Z. Q. Liu, M. E. Holtz, C. J. Li, X. Renshaw Wang, W. M. Lü, M. Notopothula, L. S. Fan, J. A. Turcaud, L. R. Dedon, C. Frederick, R. J. Xu, R. Gao, A. T. N'Diaye, E. Arenholz, J. A. Mundy, T. Venkatesan, D. A. Muller, L.-W. Wang, J. Liu, L. W. Martin, *Phys. Rev. Lett.* **2017**, *119*, 156801.
- [45] T. C. Kaspar, P. V. Sushko, S. R. Spurgeon, M. K. Bowden, D. J. Keaveny, R. B. Comes, S. Saremi, L. W. Martin, S. A. Chambers, *Adv. Mater. Interfaces* **2019**, *6*, 1801428.
- [46] M. Abbate, F. M. F. de Groot, J. C. Fuggle, A. Fujimori, O. Strelbel, F. Lopez, M. Domke, G. Kaindl, G. A. Sawatzky, M. Takano, Y. Takeda, H. Eisaki, S. Uchida, *Phys. Rev. B* **1992**, *46*, 4511.
- [47] T. Saitoh, A. E. Bocquet, T. Mizokawa, H. Namatame, A. Fujimori, M. Abbate, Y. Tabake, M. Takano, *Phys. Rev. B* **1995**, *51*, 13942.
- [48] Y. Ishida, R. Eguchi, M. Matsunami, K. Horiba, M. Taguchi, A. Chainani, Y. Senba, H. Ohashi, H. Ohta, S. Shin, *Phys. Rev. Lett.* **2008**, *100*, 056401.
- [49] P. Schütz, D. Di Sante, L. Dudy, J. Gabel, M. Stübinger, M. Kamp, Y. Huang, M. Capone, M.-A. Husanu, V. N. Strocov, G. Sangiovanni, M. Sing, R. Claessen, *Phys. Rev. Lett.* **2017**, *119*, 256404.
- [50] D. Pesquera, G. Herranz, A. Barla, E. Pellegrin, F. Bondino, E. Magnano, F. Sánchez, J. Fontcuberta, *Nat. Commun.* **2012**, *3*, 1189.
- [51] C. T. Chen, Y. U. Idzerda, H.-J. Lin, N. V. Smith, G. Meigs, E. Chaban, G. H. Ho, E. Pellegrin, F. Sette, *Phys. Rev. Lett.* **1995**, *75*, 152.
- [52] J.-H. Park, E. Vescovo, H.-J. Kim, C. Kwon, R. Ramesh, T. Venkatesan, *Phys. Rev. Lett.* **1998**, *81*, 1953.
- [53] M. R. Fitzsimmons, C. Majkrzak, *Modern Techniques for Characterizing Magnetic Materials*, Springer, New York **2005**, Ch. 2.
- [54] H. Guo, Z. Wang, S. Dong, S. Ghosh, M. Saghayezhian, L. Chen, Y. Weng, A. Herklotz, T. Z. Ward, R. Jin, S. T. Pantelides, Y. Zhu, J. Zhang, E. W. Plummer, *Proc. Natl. Acad. Sci. USA* **2017**, *114*, E5062.
- [55] E.-J. Guo, M. A. Roldan, T. Charlton, Z. Liao, Q. Zheng, H. Ambaye, A. Herklotz, Z. Gai, T. Z. Ward, H. N. Lee, M. R. Fitzsimmons, *Adv. Funct. Mater.* **2018**, *28*, 1800922.
- [56] M. M. Björck, G. Andersson, *J. Appl. Crystallogr.* **2007**, *40*, 1174.
- [57] S. J. Clark, D. S. Matthew, J. P. Chris, J. H. Pickard, I. J. P. Matt, R. Keith, C. P. Mike, *Z. Kristallogr.* **2005**, *220*, 567.
- [58] J. P. Perdew, K. Burke, M. Ernzerhof, *Phys. Rev. Lett.* **1996**, *77*, 3865.
- [59] A. J. Morris, R. J. Nicholls, C. J. Pickard, J. R. Yates, *Comput. Phys. Commun.* **2014**, *185*, 1477.
- [60] J. R. Yates, X. Wang, D. Vanderbilt, I. Souza, *Phys. Rev. B* **2007**, *75*, 195121.
- [61] A. I. Liechtenstein, V. I. Anisimov, J. Zaanen, *Phys. Rev. B* **1995**, *52*, R5467.
- [62] G. Pizzi, A. Cepellotti, R. Sabatini, N. Marzari, B. Kozinsky, *Comput. Mater. Sci.* **2016**, *111*, 218.